Bulk and surface electronic structure of Bi_4Te_3 from *GW* calculations and photoemission experiments

Dmitrii Nabok,[1] Murat Tas,[2] Shotaro Kusaka,[3] Engin Durgun [●],[4] Christoph Friedrich,[1] Gustav Bihlmayer [●],[1] Stefan Blügel [●],[1] Toru Hirahara [●],[3] and Irene Aguilera[1,*]

[1]*Peter Grünberg Institut and Institut for Advanced Simulation, Forschungszentrum Jülich, 52425 Jülich and JARA, Germany*
[2]*Department of Physics, Gebze Technical University, Kocaeli 41400, Turkey*
[3]*Department of Physics, Tokyo Institute of Technology, 2-12-1 Ookayama, Meguro-ku, Tokyo 152-8551, Japan*
[4]*UNAM–National Nanotechnology Research Center and Institute of Materials Science and Nanotechnology, Bilkent University, Ankara 06800, Turkey*

We present a combined theoretical and experimental study of the electronic structure of stoichiometric Bi_4Te_3, a natural superlattice of alternating Bi_2Te_3 quintuple layers and Bi bilayers. In contrast to the related semiconducting compounds Bi_2Te_3 and Bi_1Te_1, density functional theory predicts Bi_4Te_3 is a semimetal. In this work, we compute the quasiparticle electronic structure of Bi_4Te_3 in the framework of the *GW* approximation within many-body perturbation theory. The quasiparticle corrections are found to modify the dispersion of the valence and conduction bands in the vicinity of the Fermi energy, leading to the opening of a small indirect band gap. Based on the analysis of the eigenstates, Bi_4Te_3 is classified as a dual topological insulator with bulk topological invariants $\mathbb{Z}_2$ (1; 111) and magnetic mirror Chern number $n_M = 1$. The bulk *GW* results are used to build a Wannier-function-based tight-binding Hamiltonian that is further applied to study the electronic properties of the (111) surface. The comparison with our angle-resolved photoemission measurements shows excellent agreement between the computed and measured surface states and indicates the dual topological nature of Bi_4Te_3.

I. INTRODUCTION

The field of topological matter, both as a fundamental concept and as a search for materials for practical applications, is a very rapidly developing field [1–3]. Being based on the physics of spin-orbit coupling (SOC), topological insulators (TIs) show electronic properties fundamentally distinct from conventional insulators. Their surfaces are characterized by the existence of metallic surface states which are protected by time-reversal and spatial symmetries [4–7]. Moreover, electrons in such states are spin polarized, and their spin angular moment orientation and propagation momentum are locked to each other. This property opens promising possibilities for the generation and control of dissipationless spin currents that might be exploited in practical applications in spintronics, quantum computation, and thermoelectronics.

Bi-Te alloys present a wide group of materials with intriguing and technologically important properties. These compounds have been known and intensively studied for a long time due to their thermoelectric properties. In addition, recently, growing interest in these alloys has arisen after the discovery of nontrivial topological insulating properties that make them very promising candidates for future generation of electronic devices for spintronics and quantum computation [1].

Bi_2Te_3 is the first theoretically predicted and experimentally confirmed [1,8,9] prototype TI with surface states forming a single nondegenerate Dirac cone. It has been shown to be a strong TI (STI) with a $\mathbb{Z}_2$ invariant (1; 000) whose surface states are protected by time-reversal symmetry on all surfaces. It has been further shown that Bi_2Te_3 belongs to the family of topological crystalline insulators (TCIs) with $n_M = -1$, where the presence of mirror symmetry leads to the protection of the metallic surface states lying in the planes perpendicular to the mirror planes. Thus, Bi_2Te_3 was characterized as the first material predicted to be both a STI and a TCI. Since it exhibits this double topological nature, it was termed a dual TI [10]. With such a combination, one can potentially exploit the fact that controlled symmetry breaking would destroy certain surface states while keeping others intact.

In the quest for materials with targeted topological properties, an interesting direction of investigation is to combine layers of known topological compounds to form heterostructures [11]. For instance, an interface built by a bilayer (BL) of Bi(111) on a Bi_2Te_3 substrate has been studied as a prototype system that indeed combines properties of the two-dimensional (2D) and three-dimensional (3D) TIs such that topologically protected one-dimensional edge and 2D surface states coexist at the surface [12].

In this context, it becomes interesting to study compounds that would combine the Bi bilayers (Bi_2) and Bi_2Te_3 quintuple layers to create new stoichiometric bulk Bi-Te alloys. Bi_1Te_1, one such combination, was recently synthesized,

---

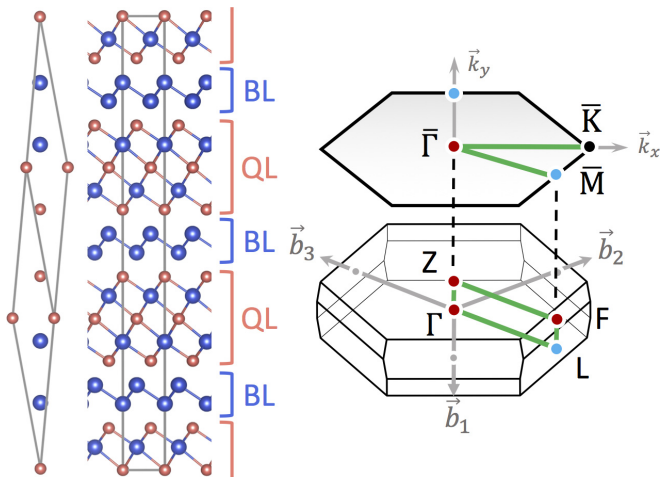*Present address: Institute of Physics, University of Amsterdam, 1012 WX Amsterdam, Netherlands. i.g.aguilerabonet@uva.nl

FIG. 1. Left: Crystal structure of Bi_4Te_3, consisting of three quintuple Bi_2Te_3 layers intercalated with three Bi_2 layers, presented in hexagonal (conventional) and rhombohedral (primitive) unit cells. Right: The Brillouin zones of the bulk crystal and the (111) surface. Time-reversal-invariant special **k** points are shown with red (plus) and blue (minus) dots reflecting the valence-state parity used to compute the topological invariant $\mathbb{Z}_2$.

characterized, and shown to be a dual 3D TI in which a weak TI phase and TCI phase appear simultaneously [13].

Bi_4Te_3 is another well-known natural superlattice of Bi_2 and Bi_2Te_3 (see Fig. 1) whose topological properties are not yet thoroughly understood. In contrast to Bi_2Te_3 and Bi_1Te_1, this compound is considered to be a topological semimetal according to the Topological Materials Database [14]. Bi_4Te_3 has been seen to undergo a number of pressure-induced structural transformations to metallic phases that lead to distinct superconducting states [15]. Saito *et al.* [16] described the Bi_4Te_3 bulk crystal taking SOC into account as a zero band gap semimetal with a Dirac cone at the Γ point. In all mentioned works, the theoretical analysis of the band structure was performed using density functional theory (DFT). By contrast, we go beyond DFT in this study and provide an analysis of the bulk and surface electronic structure of Bi_4Te_3 by employing the state-of-the-art quasiparticle *GW* approach based on many-body perturbation theory (MBPT). This technique was applied earlier to study the electronic properties of other topological materials, and the importance of quasiparticle effects has been established for these materials [17–26]. The results for the constituents of Bi_4Te_3 (i.e., Bi_2Te_3 [24] and Bi [27]) also proved that the *GW* method significantly improves the results provided by DFT. In particular, in Ref. [27], we showed with the example of Bi the difficulties in accurately describing the electronic structure of semimetals or very narrow band gap semiconductors, and we highlighted the importance of using methods beyond DFT to study these kinds of materials accurately. Since Bi_4Te_3 contains layers of Bi, it is not surprising that one needs to resort to the *GW* method to predict the fine details of its electronic structure. In our approach, we perform *GW* calculations for the bulk, and in order to compute the surface electronic band structure, we further parametrize a tight-binding (TB) Hamiltonian with the help of Wannier functions [28]. The TB Hamiltonian is obtained

by following the method described in Ref. [26], and thus, it is calculated fully *ab initio* without the need for adjustable parameters. The calculation of bulk and surface states as well as surface resonances with this method allows us to provide a direct comparison between the computed spectra and results from the angle-resolved photoemission spectroscopy (ARPES) studies.

The structure of this work is as follows. We start with the description of the crystal structure of Bi_4Te_3 in Sec. II. Then we provide details of the theoretical (Sec. III) and experimental (Sec. IV) setups. In Sec. V A, we characterize the bulk electronic structure and compare it with previous works. Then, in Sec. V B, we present the surface band structure and analyze the dual topological nature of Bi_4Te_3, including its $\mathbb{Z}_2$ topological index. In Sec. VI, we perform a comparative analysis of the theoretical and experimental results. Finally, we conclude in Sec. VII.

II. CRYSTAL STRUCTURE

The lattice structure of bulk Bi_4Te_3 is built as a stack of quintuple layers (QLs) of Bi_2Te_3 intercalated with Bi bilayers with a periodic crystal structure that can be expressed as $[(Bi_2)(Bi_2Te_3)]_3$. Both conventional and primitive unit cells are shown in Fig. 1. The primitive cell reflects the rhombohedral crystal symmetry (space group R-$3m$) and consists of seven atoms (with two Te and two Bi nonequivalent atoms). We employ the experimental lattice parameters of [29]. The primitive cell is determined by $a_{rho} = 14.197$ Å and $\alpha = 18.0374°$, or, using the conversion to the conventional (hexagonal) cell, $a_{hex} = a_{rho}\sqrt{2(1 - \cos\alpha)} = 4.451$ Å and $c_{hex} = a_{rho}\sqrt{3(1 + 2\cos\alpha)} = 41.888$ Å. Optimization of the crystal structure (for details, see the Supplemental Material [30]) has revealed the lattice constants are very close to the experimental ones: $a_{rho}^{opt} = 14.091$ Å and $\alpha^{opt} = 18.1385°$. The optimized structure has a slightly (0.1 Å) smaller interlayer distance, which, keeping in mind the van der Waals type of bonding, has only a little influence on the electronic band structure (see Fig. 1 in the Supplemental Material [30]). Hence, in the following, the results are obtained with the experimental lattice parameters given above.

III. COMPUTATIONAL DETAILS

The electronic quasiparticle band structure is computed using the G_0W_0 approximation of the MBPT. The calculations are performed employing the code SPEX [31], which implements the *GW* technique in the full-potential linearized augmented plane-wave (FLAPW) framework. The starting point for the *GW* calculations is provided through an interface with the FLAPW DFT code FLEUR [32]. The generalized gradient approximation in the Perdew-Burke-Ernzerhof (PBE) parametrization [33] is chosen for the exchange-correlation potential. The core electrons are treated fully relativistically by solving the Dirac equation with the spherically averaged effective potential around each nucleus. For the valence electrons, space is partitioned into muffin-tin (MT) spheres and an interstitial region; in the former we use an angular momentum cutoff of $l_{max} = 10$, and in the latter we us a plane-wave cutoff of 3.6 bohr^{-1}. The MT radii are set to 2.8 bohrs for all atoms.

An $8 \times 8 \times 8$ **k**-point grid was used to sample the Brillouin zone.

The quasiparticle corrections are computed with the inclusion of SOC, which is known to have an important impact on the electronic properties of topological materials such as Bi_2Te_3 [22]. SOC is already included in the ground state Kohn-Sham (KS) calculations; the KS eigenfunctions are thus single-particle spinor wave functions. We employ the second-variation technique [34], in which the SOC Hamiltonian is set up and diagonalized in the basis of KS states that have been precomputed without SOC. Specifically for this basis, we use the 400 KS states with the lowest energy, which, in combination with other computational parameters, results in KS eigenenergies being converged within 2 meV.

SPEX makes use of the auxiliary mixed product basis for representing matrix elements of the nonlocal operators. Based on our earlier experience [20] as well as performed convergence tests, we use the following parameters for the *GW* calculation. The mixed product basis is constructed by setting the maximal angular momentum for the muffin-tin spheres to $L = 5$ and $G_{max} = 3.0$ bohr^{-1} for the interstitial part. For an accurate representation of the unoccupied states in the FLAPW method, additional basis functions (so-called local orbitals) are included, two functions in each angular momentum channel with $l \leqslant 3$. A total of about 1000 states (giving rise to about 880 empty states) corresponding to a maximal cutoff energy of ≈ 86 eV are included for computing the screened Coulomb potential and the correlation self-energy. The Brillouin zone (BZ) integration is performed on an $8 \times 8 \times 8$ Monkhorst-Pack **k**-point mesh. The contour deformation technique is used for the frequency convolution integration with 29 nonequidistant frequency points up to an (imaginary) energy of 272 eV along the imaginary axis. The self-energy is evaluated on a uniform grid with an increment of 0.54 eV along the real axis. Between the grid points, we employ spline interpolation. In this way, the self-energy is given as a continuous function along the real frequency axis, which allows us to solve the quasiparticle equation, which is nonlinear in frequency, without resorting to a linearization of the self-energy. The *GW* computational setup has been checked to provide the quasiparticle energies converged to within 15 meV. It should be mentioned that a $6 \times 6 \times 6$ **k**-point grid would be sufficient to reach reasonable energy convergence. However, such a grid turned out to be too coarse for an accurate Wannier interpolated band structure.

The Wannier-function-based TB Hamiltonian is used further as an input to compute the surface projected electronic band structure employing the WANNIERTOOLS [35] program package. In this work, we are interested in a narrow region of bands lying close to the Fermi level. These bands have a predominant *p* character, which motivates us to set *p*-type "initial-guess" Wannier functions for each inequivalent atom and to perform the maximal localization procedure via an interface with the WANNIER90 library [36].

IV. EXPERIMENTAL DETAILS

The samples were fabricated by the following procedure. First, a clean Si(111)-7 $\times$ 7 surface was prepared on an *n*-type substrate by a cycle of resistive heat treatments. Then, Bi was
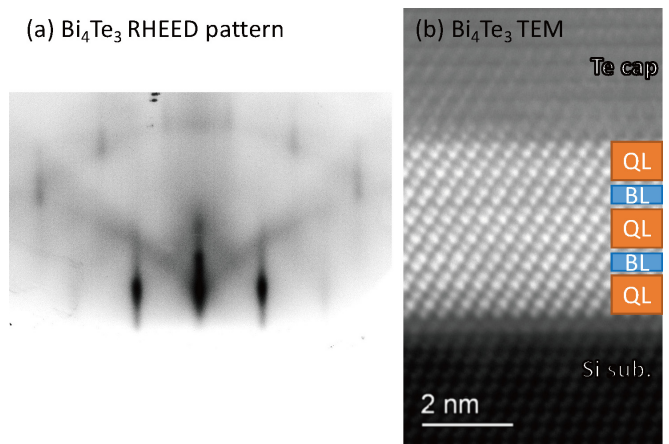

FIG. 2. (a) RHEED pattern and (b) TEM image of the $Bi_4Te_3(111)$ film with the QL termination.

deposited on the 7 $\times$ 7 structure at 250°C under Te-rich conditions. Such a procedure is reported to result in high-quality $Bi_2Te_3(111)$ film formation [37]. Then, the grown films were annealed at 310°C for 2 h in ultrahigh vacuum. During this process, Te was desorbed from the sample, and thus, the sample became a $Bi_4Te_3(111)$ film with the QL termination, as confirmed by transmission electron microscopy (TEM) observations. Figure 2 shows the reflection high-energy electron diffraction (RHEED) pattern and the TEM image of a typical sample. The in-plane lattice constant was determined to be 4.45 ± 0.05 Å, and the films were determined to be two unit cells thick with an additional QL at the interface between the film and the substrate (or the wetting layer). Details of the sample preparation and structure characterization will be published elsewhere [38]. The ARPES measurements were performed *in situ* after the sample preparation with a commercial hemispherical photoelectron spectrometer equipped with angle and energy multidetections (MBS A1) at UVSOR BL-7U of UVSOR-III with $h\nu = 20$ eV photons [39]. The sample was cooled down to 16 K for the measurements.

V. RESULTS

A. Bulk band structure

The electronic band structure of Bi_4Te_3 is presented in Fig. 3. The PBE band structure indicates that Bi_4Te_3 is a semimetal with a wide electron pocket along the *Z-F* **k**-point path and a small hole pocket around the *Z* point. The valence (VB) and conduction (CB) bands closely approach each other at Γ, where a band inversion takes place [see Fig. 3(b)]. In contrast to our results, the band structure presented in the Topological Materials Database [14] seems to exhibit a crossing of the VB and CB along the Γ-*Z* in the vicinity of the Fermi level. On the other hand, our DFT band structure is in good agreement with that of Ref. [16]. Our calculation yields an energy gap of 10 meV between the VB and CB at the Γ point, and the CB minimum at this point is located slightly below the Fermi energy. The value of the gap turns out to be quite sensitive to the computational parameters. As shown in the Supplemental Material [30], the magnitude of the
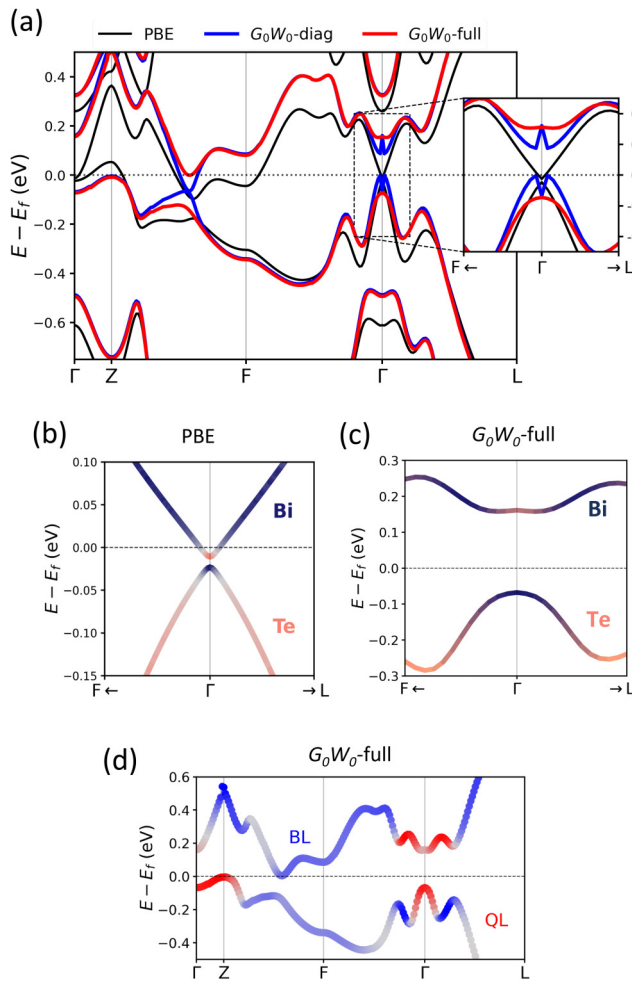
FIG. 3. (a) Electronic band structure of Bi_4Te_3 in the vicinity of the Fermi energy as computed with different methods: "diag" refers to the standard G_0W_0 computational approach, and "full" refers to the results obtained by including the off-diagonal matrix elements of the self-energy. The band structures are calculated explicitly on a fine mesh along the **k** path, *not* with Wannier interpolation. The bands are aligned with respect to the Fermi energy. The inset shows the behavior of the valence and conduction states in the vicinity of Γ. (b) and (c) The band inversion between the valence and conduction states at the Γ point calculated with PBE and G_0W_0-full, respectively. The color of the lines represents the contribution of Bi and Te atoms. (d) G_0W_0-full valence and conduction bands projected onto the BL (blue) and QL (red).

FIG. 4. Comparison of the explicit and Wannier-interpolated electronic band structures of Bi_4Te_3 in the vicinity of the Fermi level.

gap depends on the choice of the local orbital basis functions employed in the FLAPW method.

Adding the quasiparticle corrections following the standard G_0W_0 approach by taking into account only the diagonal matrix elements of the self-energy (blue lines, labeled "diag" in Fig. 3) modifies the described behavior of the KS bands significantly. The quasiparticle band structure is computed on a fine **k** mesh along the BZ path explicitly. (For comparison, we present the band structure obtained with the Wannier interpolation [36] in Fig. 4.) The gap between the VB and CB at Γ strongly increases and reaches a value of ≈ 0.2 eV. Overall, the CB is shifted up in energy in the entire BZ except
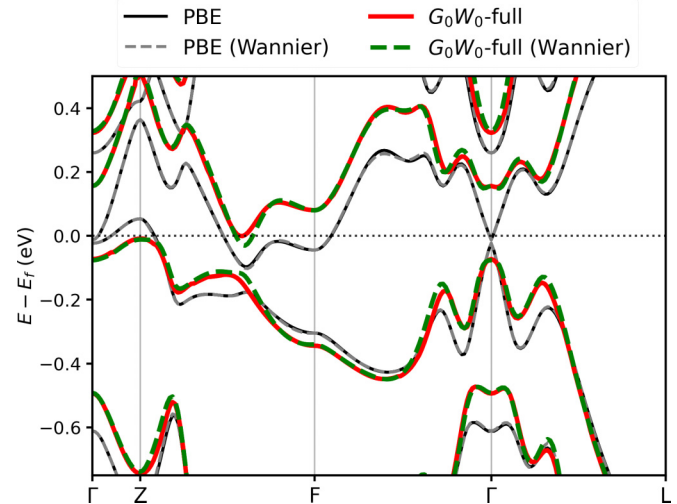
in a tiny area around the middle of the *Z-F* line where a narrow electron pocket remains. In contrast, the VB does not show a uniform energy shift. It is shifted below the Fermi level along Γ-*Z*. In this way, the hole pocket predicted by PBE disappears. At the same time, the VB is shifted up closer to the Fermi level around the middle of the *Z-F* path, where it almost touches the CB.

Looking closer at the behavior of the VB and CB at Γ [inset of Fig. 3(a)], one notices a characteristic anomaly: both bands show sharp narrow spikes in the energy dispersion. This unphysical anomaly was observed earlier in the G_0W_0 band structure of the closely related topological material Bi_2Te_3 [20]. The anomaly is caused by the neglect of off-diagonal elements of the self-energy matrix, which play an important role in these materials due to strong hybridization effects caused by the SOC operator. The relativistic mass enhancement and the SOC are responsible for the band inversion of the VB and CB in the vicinity of Γ. The band inversion manifests itself in a mixture of electronic states of different orbital natures, as can be seen from the atom-projected band structure shown in Figs. 3(b) and 3(c). In the vicinity of the BZ center, the VB is predominantly formed by the *p* states of Te (light pink), whereas the CB consists of *p* states of Bi (dark blue). But in a small region around Γ, the VB and CB orbital characters are reversed. Due to the different band dispersions in G_0W_0 around Γ, the reversal of orbital character takes place in a different region of reciprocal space, much smaller in PBE [Fig. 3(b)] than in G_0W_0 [Fig. 3(c)]. Thus, for a proper description, the off-diagonal self-energy matrix elements need to be taken into account because only then can the quasiparticle wave functions be different from the KS eigenfunctions. Neglecting this state mixing in G_0W_0 by treating only diagonal elements of the self-energy (G_0W_0-diag) leads to the unphysical behavior of the quasiparticle bands around Γ shown by the blue lines in Fig. 3(a). As is evidenced by the red lines instead (labeled "full"), the inclusion of the off-diagonal matrix elements of the self-energy immediately recovers a physically meaningful dispersion of the bands close to Γ. Another important modification that is induced by the

treatment of the off-diagonal components is along the Z-F path. Instead of an effective attraction like in the case of G_0W_0-diag, the VB and CB repel each other such that the electron pocket (and thus the semimetallic character) disappears, and a fundamental indirect band gap of 10 meV opens between the valence band maximum at Z and conduction band minimum along Z-F. A comparison of the red and blue curves in Fig. 3(a) thus highlights the importance of taking into account the hybridization caused by many-body self-energy effects to describe the electronic properties of topological materials reliably.

Since Bi_4Te_3 consists of alternating BLs and QLs, it is also interesting to look at the corresponding state projections. In the G_0W_0-full approach [20], the quasiparticle states are represented as linear combinations of KS states, which allows us to analyze the orbital character of the quasiparticle states beyond DFT [as done in Fig. 3(c) to visualize the band inversion]. As one can see in Fig. 3(d), the absolute VB maximum and the local maximum at Γ are formed by QL states, whereas the rest of the VB is mostly formed by BL states. The CB in the vicinity of Γ is also formed predominantly by QL states, but there is a noticeable contribution of BL states directly at Γ.

Before we proceed with the analysis of the surface band structure based on the TB Hamiltonian, we comment on the performance of the Wannier interpolation. For this purpose, the PBE and G_0W_0-full interpolated band structures are compared in Fig. 4 with corresponding results obtained from explicit calculations on a fine mesh along a high-symmetry **k** path. In both cases, the interpolated curves are very close to the explicit ones. However, in the G_0W_0-full case, there is a small deviation along Z-F, where the interpolated CB forms a tiny electron pocket, whereas the explicitly calculated CB does not. We note that the Fermi energy is calculated with the $8 \times 8 \times 8$ **k**-point set. Any band dispersion feature that falls between the **k** points, like the electron pocket in the Wannier-interpolated band structure, is not taken into account in the determination of the Fermi energy.

B. Surface band structure

Due to relatively weak coupling between the QLs and BLs, the (111) plane in the rhombohedral lattice [the (001) plane in the hexagonal definition] is the surface with the lowest surface energy. The (111) cleavage plane induces either a QL or a BL surface termination. The TB parametrization of the G_0W_0-full band structure with the help of the Wannier functions has been shown to be a very powerful tool to study surface states of topological materials [26]. Following this technique, in Figs. 5(a) and 5(b) we present electronic band structures for a semi-infinite film obtained with the iterative Green's function method [40] as implemented in WANNIERTOOLS [35]. The color code reflects the localization rate of the states at the topmost surface layer such that the bright narrow bands are the emerging surface states in each termination. Results are shown along the surface BZ path shown in Fig. 1 for both QL and BL terminations. Figures 5(c) and 5(d) present instead the GW-TB electronic surface structure for a finite slab [18 (QL+BL) layers]. As one can see from a comparison of the semi-infinite and finite spectra, the 18-double-layer slab is sufficient to reproduce all details of the semi-infinite surface
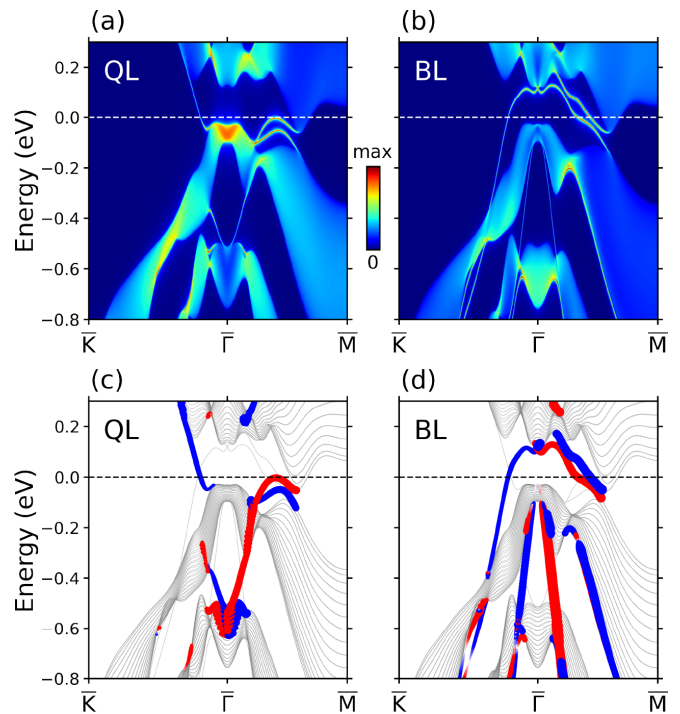

FIG. 5. GW-TB electronic structure of the semi-infinite Bi_4Te_3 (111) surface terminated either (a) on the QL or (b) on the BL. The color map corresponds to the density of states projected on the topmost layer in each termination. Emerging surface states are represented as narrow bands arising in different parts of the spectra outside of the wide bulk states. (c) and (d) GW-TB electronic structure of the 18 (QL+BL) layer slab. The surface states with localization on either the topmost (c) QL or (d) BL levels are highlighted with colored circles. The size and color of the circles correspond to the magnitude and sign (red for positive and blue for negative) of the in-plane component of the spin polarization perpendicular to the momentum.

structure. This is in agreement with the conclusion of Ref. [41] that only a few layers are necessary to converge to the bulk behavior. The surface states with predominant localization on the lowest QL [Fig. 5(c)] and the topmost BL [Fig. 5(d)] in the slab are highlighted with circles whose size and color correspond to the magnitude and in-plane orientation (red for positive and blue for negative) of the spin polarization perpendicular to the surface momentum.

The surface state dispersion patterns are remarkably distinct in both terminations. In the QL case, the surface states are dispersing upward in energy when moving away from the BZ center, whereas in the BL terminations the surface states have a downward dispersion. This behavior closely resembles the behavior in analogous studies on Bi_1Te_1 [13]. The surface states cross the Fermi level in both terminations, which already suggests a nontrivial topological nature of the material. Indeed, there is a single surface state crossing the Fermi level along the $\overline{\Gamma}$-$\overline{K}$ path in both terminations. It is different along $\overline{\Gamma}$-$\overline{M}$, where both states are located below the Fermi level in the QL termination and cross the Fermi level in the BL termination. It is important to point out that only one surface state in the pair connects the VB and CB bulk bands and thus can be considered topologically nontrivial. Moreover, the topologically nontrivial band in the QL termination
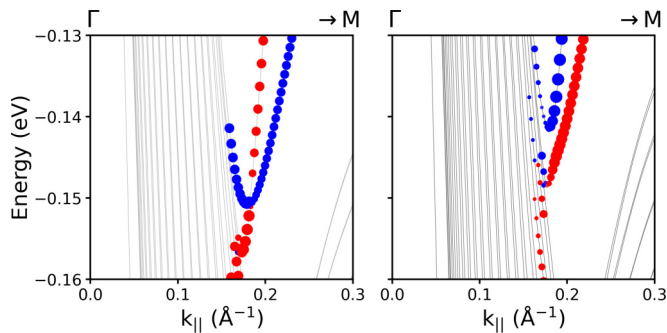
FIG. 6. PBE electronic structure of the 18 (QL+BL) layer slab in the vicinity of the surface state crossing point along $\overline{\Gamma}$-$\overline{M}$ for the symmetric (left) and deformed (right) Bi$_4$Te$_3$. Only the QL surface states are treated. The color code of the circles is as in Fig. 5.

approaches the Fermi level at its maximum along $\overline{\Gamma}$–$\overline{M}$ very closely. Disregarding the fact that the bulk material still has a small density of states at the Fermi energy, Bi$_4$Te$_3$ reveals topological features that are distinctive for a strong topological material. Since the material crystal symmetry contains an inversion center, the $\mathbb{Z}_2$ topological invariants are readily calculated from the valence-state parities at the time-reversal-invariant momenta (TRIMs) [4]. The parity invariants for each bulk TRIM K_i are shown in Fig. 1, where the colors of the red (blue) dots correspond to the signs of the valence-state parity eigenvalue products $\delta(K_a) = + (-1)$. Based on the parity invariants, we obtain $\mathbb{Z}_2 = (1; 111)$, which characterizes Bi$_4$Te$_3$ as a strong topological material similar to Sb or Bi$_{1-x}$Sb$_x$ [42]. According to its $\mathbb{Z}_2$, one expects an odd number of surface states crossing the Fermi level and the presence of an electron pocket surrounding Γ, which is perfectly supported by our simulations. Our electronic band structure differs from the one presented in the Topological Materials Database [14]. As a consequence and in contrast to our findings, one would deduce $\mathbb{Z}_2 = (0; 111)$ from the data of Ref. [14], which would characterize Bi$_4$Te$_3$ as a weak topological material. Therefore, experimental studies are required to back up either of the theoretical predictions.

In addition to the mentioned behavior of the surface states, there are three important features that are revealed in Fig. 5. First, there is a crossing between a pair of surface states in the QL termination along $\overline{\Gamma}$-$\overline{M}$. The crossing is located at an energy of about -0.1 eV in the close vicinity of the bulk state continuum. This feature has motivated us to study another topological invariant that characterizes the behavior of the surface states in the presence of mirror symmetry, the magnetic mirror Chern number n_M [5,10,42]. The result $n_M = 1$ confirms the existence of a single surface state which connects the valence and conduction bands and can potentially lead to a crossing of the two surface bands. The physical picture is similar to the analogous situation in Bi$_{1-x}$Sb$_x$ [42], where the same value of $n_M = 1$ was shown to be a marker of the band crossing. The mirror Chern number can have a nonzero value only if the crystal possesses a mirror plane. Therefore, as a check, we have slightly strained the crystal along the $\mathbf{b}_{hex}$ hexagonal axis and thus destroyed the mirror plane. In Fig. 6 we compare the behavior of the surface states in the vicinity of the discussed crossing point in the symmetric and deformed Bi$_4$Te$_3$ crystals. For demonstration purposes, we have computed the PBE surface band structures for an 18 (QL+BL) layer slab. As seen from the left panel of Fig. 6, the crossing takes place at $k_{||} \approx 0.18$ Å^{-1} in the crystal with the mirror plane. In the deformed crystal (right panel), the states are shifted with respect to each other such that no crossing occurs. An equivalent crossing has been observed in the surface states of Bi$_1$Te$_1$ along the same path and at approximately the same momentum [13].

The second feature to be discussed is a Dirac-cone-like crossing located in the BL termination at Γ at an energy of about 0.1 eV above the Fermi energy, slightly below the bulk conduction band minimum. The existence of this Dirac point for the BL termination can also be understood by looking at the system of one bilayer of Bi deposited on Bi$_2$Te$_3$ [12]. As in Bi/Bi$_2$Te$_3$, there seems to be a charge transfer from the BL to the QL. This shifts the Dirac cone above the Fermi level. There is one important consequence now in terms of the band crossing along $\overline{\Gamma}$-$\overline{M}$: Since the mirror Chern number is positive, the lowest of the two spin-split surface states connects the valence band to the conduction band [42]. When the Dirac
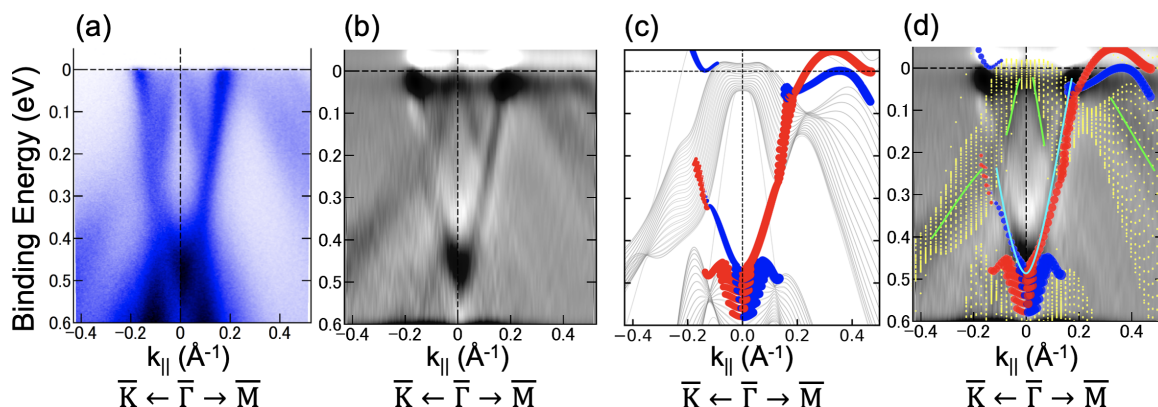

FIG. 7. (a) and (b) ARPES spectra of the Bi$_4$Te$_3$ QL terminated (111) surface. (a) shows the raw data, and (b) shows the second derivative with respect to energy to enhance spectral features. (c) The same plot as in Fig. 5(c) (*GW*-TB) shifted up 50 meV. (d) Comparison between the experimental and (shifted) theoretical electronic surface structures. Yellow dots represent computed bulk states. As a guide to the eye, solid lines highlight the dispersion of the most intensive ARPES peaks.
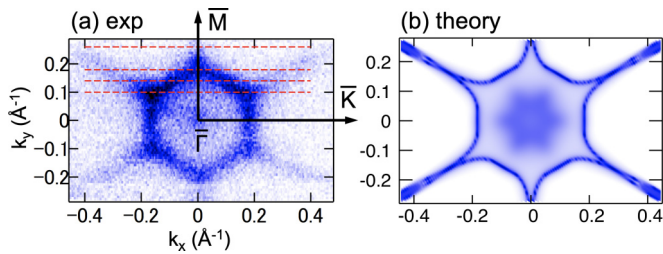
FIG. 8. $k_{\|,x}$ versus $k_{\|,y}$ (a) experimental and (b) computed (*GW*-TB) Fermi surface maps. Red dashed lines show constant $k_{\|,y}$ scans presented in Fig. 9.

point is below the Fermi level [QL case in Fig. 5(c)], there is a band crossing of the two surface states. When, instead, the Dirac cone is above the Fermi level [BL case in Fig. 5(d)], no crossing appears.

A third Dirac-cone feature comes from the Dirac cone of Bi$_2$Te$_3$. This can be seen as a Dirac-cone crossing at $\overline{\Gamma}$ below the Fermi level (≈ -0.55 eV) for the QL termination. The Dirac cone seems to be resonant with the bulk continuum [Fig. 5(a)] and reveals itself better in Fig. 5(c) for the finite slab as a strongly spin-polarized feature.

VI. SURFACE ELECTRONIC STRUCTURE MEASURED BY ARPES

Figures 7(a) and 7(b) present the experimental spectrum of the QL terminated (111) surface of a thin film of Bi$_4$Te$_3$ as measured by ARPES for two directions. For compari-

son with the experiment, theoretical bands have been shifted 50 meV upward in Fig. 7(c). An overlay of the two electronic structures in Fig. 7(d) shows good agreement between the experimental and theoretical spectra. The comparison makes it possible to distinguish the features from the bulklike states (yellow dots) and from the surface states (red and blue circles). Thus, the experimental bands marked with green lines in Fig. 7(d) correspond to bulk states. The sharp parabolic shaped line (turquoise) is the surface state equivalent to the one that can be observed in Bi$_2$Te$_3$ [12] and Bi$_1$Te$_1$ [13]. Note that although this band disperses sharply all the way up to the Fermi level for the $\overline{\Gamma}$-$\overline{M}$ direction, its intensity is weak along the $\overline{\Gamma}$-$\overline{K}$ direction at 0.1–0.2 eV due to the strong hybridization with the bulk states. The experimental spectrum also reveals an additional band along $\overline{\Gamma}$-$\overline{M}$ with a binding energy of ≈ 30 meV. As indicated in the theoretical spectrum, this is the second surface state that crosses the paraboliclike surface state, as discussed in Sec. V B. This crossing is an important marker of the topological crystalline nature of Bi$_4$Te$_3$. To confirm that the crossing does take place, the ARPES spectra were recorded along the nonsymmetry lines along k_x (parallel to $\overline{\Gamma}$-$\overline{K}$) for different values of k_y, as is sketched in Fig. 8 with red dashed lines. These spectra are shown and compared to the corresponding theoretical band structures in Fig. 9. Following from Figs. 9(c)–9(e), the Dirac-cone crossing likely occurs around $k_y = 0.18$ Å^{-1}. The Fermi surface of the thin-film Bi$_4$Te$_3$ shown in Fig. 8 has a hexagonal shape surrounding the Γ point with straight branches going outward at each corner. A similar shape is obtained in the *GW*-TB simulations. Sharp lines correspond to the crossing of the isoenergy surface
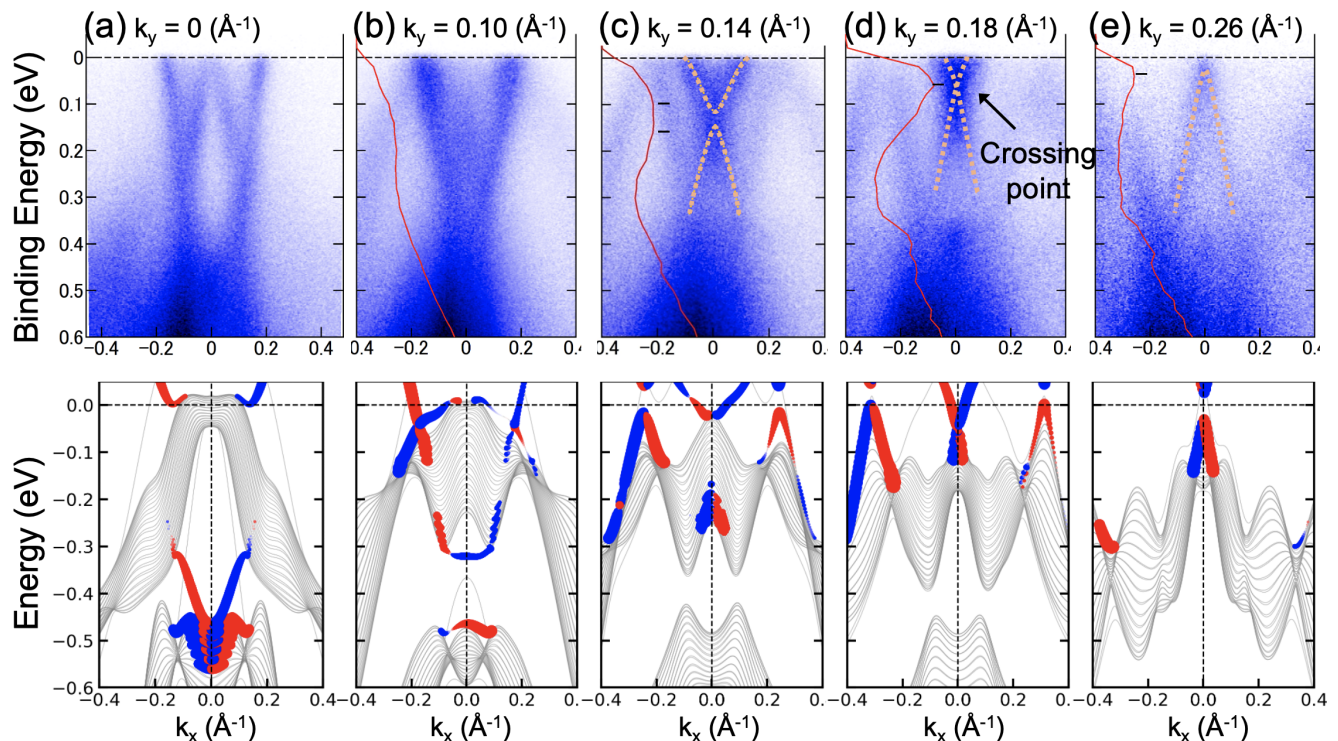

FIG. 9. Electronic structure of Bi$_4$Te$_3$ along the nonsymmetry lines shown in Fig. 8. Experimental (50 meV shifted theoretical) spectra for (a) $k_y = 0$ Å^{-1}, (b) $k_y = 0.1$ Å^{-1}, (c) $k_y = 0.14$ Å^{-1}, (d) $k_y = 0.18$ Å^{-1}, and (e) $k_y = 0.26$ Å^{-1} are shown in the top (bottom) row. The color coding in the theoretical *GW*-TB spectra is the same as in Fig. 5(c). Dashed lines indicate the experimental surface band dispersion in the vicinity of the crossing point.

with the surface states. The form of the Fermi surface is as expected from the $\mathbb{Z}_2$ classification (see, e.g., Fig. 6(a) of Ref. [42]).

VII. SUMMARY

We have performed a combined theoretical and experimental study of the electronic structure of Bi_4Te_3. Like its closely related compounds Bi_2Te_3 and Bi_1Te_1, Bi_4Te_3 is a dual topological material: a strong topological insulator with a $\mathbb{Z}_2$ invariant equal to $(1; 111)$ and a topological crystalline insulator with mirror Chern number $n_M = 1$. The semimetallic ground state predicted in DFT changes into a small indirect band gap semiconductor upon inclusion of the quasiparticle corrections in the framework of the G_0W_0 approximation of many-body perturbation theory.

We discussed how inclusion of off-diagonal matrix elements of the electronic self-energy is important for capturing the fine details of the hybridization of states due to the strong spin-orbit coupling. This hybridization between many-body states is responsible for the gap opening in Bi_4Te_3.

Theoretical analysis of Bi_4Te_3 films revealed topologically nontrivial surface states. The presence and dispersion of these states are consistent with ARPES measurements of a QL terminated Bi_4Te_3 thin film. Both theory and experiment evidence a Dirac crossing between the surface states in the valence region. This crossing is attributed to the presence of mirror symmetry and a corresponding nontrivial value of the mirror Chern number.

Note added. Recently, we became aware of a similar work reporting the electronic structure in bulk Bi_4Te_3 crystals [43].

[1] M. Z. Hasan and C. L. Kane, Rev. Mod. Phys. **82**, 3045 (2010).

[2] J. E. Moore, Nature (London) **464**, 194 (2010).

[3] X.-L. Qi and S.-C. Zhang, Rev. Mod. Phys. **83**, 1057 (2011).

[4] L. Fu and C. L. Kane, Phys. Rev. B **76**, 045302 (2007).

[5] L. Fu, Phys. Rev. Lett. **106**, 106802 (2011).

[6] T. L. Hughes, E. Prodan, and B. A. Bernevig, Phys. Rev. B **83**, 245132 (2011).

[7] F. Schindler, A. M. Cook, M. G. Vergniory, Z. Wang, S. S. P. Parkin, B. A. Bernevig, and T. Neupert, Sci. Adv. **4**, eaat0346 (2018).

[8] H. Zhang, C.-X. Liu, X.-L. Qi, X. Dai, Z. Fang, and S.-C. Zhang, Nat. Phys. **5**, 438 (2009).

[9] Y. L. Chen, J. G. Analytis, J.-H. Chu, Z. K. Liu, S.-K. Mo, X. L. Qi, H. J. Zhang, D. H. Lu, X. Dai, Z. Fang, S. C. Zhang, I. R. Fisher, Z. Hussain, and Z.-X. Shen, Science **325**, 178 (2009).

[10] T. Rauch, M. Flieger, J. Henk, I. Mertig, and A. Ernst, Phys. Rev. Lett. **112**, 016802 (2014).

[11] I. Belopolski *et al.*, Sci. Adv. **3**, e1501692 (2017).

[12] T. Hirahara, G. Bihlmayer, Y. Sakamoto, M. Yamada, H. Miyazaki, S.-I. Kimura, S. Blügel, and S. Hasegawa, Phys. Rev. Lett. **107**, 166801 (2011).

[13] M. Eschbach, M. Lanius, C. Niu, E. Młyńczak, P. Gospodarič, J. Kellner, P. Schüffelgen, M. Gehlmann, S. Döring, E. Neumann, M. Luysberg, G. Mussler, L. Plucinski, M. Morgenstern, D. Grützmacher, G. Bihlmayer, S. Blügel, and C. M. Schneider, Nat. Commun. **8**, 14976 (2017).

[14] Topological Materials Database, https://www.topologicalquantumchemistry.com.

[15] J. R. Jeffries, A. L. Lima Sharma, P. A. Sharma, C. D. Spataru, S. K. McCall, J. D. Sugar, S. T. Weir, and Y. K. Vohra, Phys. Rev. B **84**, 092505 (2011).

[16] Y. Saito, P. Fons, K. Makino, K. V. Mitrofanov, F. Uesugi, M. Takeguchi, A. V. Kolobov, and J. Tominaga, Nanoscale **9**, 15115 (2017).

[17] E. Kioupakis, M. L. Tiago, and S. G. Louie, Phys. Rev. B **82**, 245203 (2010).

[18] O. V. Yazyev, E. Kioupakis, J. E. Moore, and S. G. Louie, Phys. Rev. B **85**, 161101(R) (2012).

[19] I. A. Nechaev, R. C. Hatch, M. Bianchi, D. Guan, C. Friedrich, I. Aguilera, J. L. Mi, B. B. Iversen, S. Blügel, P. Hofmann, and E. V. Chulkov, Phys. Rev. B **87**, 121111(R) (2013).

[20] I. Aguilera, C. Friedrich, G. Bihlmayer, and S. Blügel, Phys. Rev. B **88**, 045206 (2013).

[21] I. A. Nechaev and E. V. Chulkov, Phys. Rev. B **88**, 165135 (2013).

[22] I. Aguilera, C. Friedrich, and S. Blügel, Phys. Rev. B **88**, 165136 (2013).

[23] I. P. Rusinov, I. A. Nechaev, and E. V. Chulkov, JETP Lett. **98**, 397 (2013).

[24] M. Michiardi, I. Aguilera, M. Bianchi, V. E. de Carvalho, L. O. Ladeira, N. G. Teixeira, E. A. Soares, C. Friedrich, S. Blügel, and P. Hofmann, Phys. Rev. B **90**, 075105 (2014).

[25] I. A. Nechaev, I. Aguilera, V. De Renzi, A. di Bona, A. Lodi Rizzini, A. M. Mio, G. Nicotra, A. Politano, S. Scalese, Z. S. Aliev, M. B. Babanly, C. Friedrich, S. Blügel, and E. V. Chulkov, Phys. Rev. B **91**, 245123 (2015).

[26] I. Aguilera, C. Friedrich, and S. Blügel, Phys. Rev. B **100**, 155147 (2019).

[27] I. Aguilera, C. Friedrich, and S. Blügel, Phys. Rev. B **91**, 125129 (2015).

[28] A. A. Mostofi, J. R. Yates, Y.-S. Lee, I. Souza, D. Vanderbilt, and N. Marzari, Comput. Phys. Commun. **178**, 685 (2008).

[29] K. Yamana, K. Kihara, and T. Matsumoto, Acta Crystallogr., Sect. B **35**, 147 (1979).

[30] See Supplemental Material at http://link.aps.org/supplemental/10.1103/PhysRevMaterials.6.034204 for further computational details.

[31] C. Friedrich, S. Blügel, and A. Schindlmayr, Phys. Rev. B **81**, 125102 (2010).

[32] FLEUR, http://www.flapw.de.

[33] J. P. Perdew, K. Burke, and M. Ernzerhof, Phys. Rev. Lett. **77**, 3865 (1996).

[34] C. Li, A. J. Freeman, H. J. F. Jansen, and C. L. Fu, Phys. Rev. B **42**, 5433 (1990).

[35] Q. Wu, S. Zhang, H.-F. Song, M. Troyer, and A. A. Soluyanov, Comput. Phys. Commun. **224**, 405 (2018).

[36] G. Pizzi *et al.*, J. Phys.: Condens. Matter **32**, 165902 (2020).

[37] G. Wang, X.-G. Zhu, Y.-Y. Sun, Y.-Y. Li, T. Zhang, J. Wen, X. Chen, K. He, L.-L. Wang, X.-C. Ma, J.-F. Jia, S. B. Zhang, and Q.-K. Xue, Adv. Mater. **23**, 2929 (2011).

[38] S. Kusaka, T. Sasaki, K. Sumida, S. Ichinokura, S.-I. Ideta, K. Tanaka, K. Hono, and T. Hirahara (unpublished).

[39] S.-I. Kimura, T. Ito, M. Sakai, E. Nakamura, N. Kondo, T. Horigome, K. Hayashi, M. Hosaka, M. Katoh, T. Goto, T. Ejima, and K. Soda, Rev. Sci. Instrum. **81**, 053104 (2010).

[40] M. P. L. Sancho, J. M. L. Sancho, and J. Rubio, J. Phys. F **14**, 1205 (1984).

[41] T. Chagas, G. A. S. Ribeiro, P. H. R. Gonçalves, L. Calil, W. S. Silva, Â. Malachias, M. S. C. Mazzoni, and R. Magalhães-Paniago, Electron. Struct. **2**, 015002 (2020).

[42] J. C. Y. Teo, L. Fu, and C. L. Kane, Phys. Rev. B **78**, 045426 (2008).

[43] T. Chagas, O. A. Ashour, G. A. S. Ribeiro, W. S. Silva, Z. Li, S. G. Louie, R. Magãlhaes-Paniago, and Y. Petroff, Phys. Rev. B **105**, L081409 (2022).